Spin excitations in nanometric magnetic dots: calculations and comparison with light scattering measurements

2007 J. Phys.: Condens. Matter 19 225008

(http://iopscience.iop.org/0953-8984/19/22/225008)

IOP PUBLISHING JOURNAL OF PHYSICS: CONDENSED MATTER

J. Phys.: Condens. Matter **19** (2007) 225008 (22pp) doi:10.1088/0953-8984/19/22/225008

Spin excitations in nanometric magnetic dots: calculations and comparison with light scattering measurements

Loris Giovannini[1], **Federico Montoncello**[1], **Roberto Zivieri**[2] **and Fabrizio Nizzoli**[1]

[1] Department of Physics, University of Ferrara, via G Saragat 1, I-44100 Ferrara, Italy
[2] CNISM, Research Unit of Ferrara, c/o Department of Physics, University of Ferrara, via G Saragat 1, I-44100 Ferrara, Italy

Received 12 October 2006
Published 14 May 2007
Online at stacks.iop.org/JPhysCM/19/225008

Abstract

Recent theoretical results obtained in the field of spin excitations in nanometric magnetic dots are reviewed. The dynamical matrix method and analytical approaches are described and applied to the cases of circular and elliptical planar permalloy dots. For discs, the spin dynamics in the vortex and saturated states is investigated. For saturated ellipses, the dependence of frequencies and mode profiles is studied as a function of the direction of the in-plane applied field and dot eccentricity. The results allow us to interpret Brillouin scattering data in terms of mode symmetry and localization.

(Some figures in this article are in colour only in the electronic version)

1. Introduction

The study of the equilibrium magnetic configurations and of the spin excitations in ferromagnetic planar particles on the nanoscale has considerably grown in recent years [1]. This topic is very interesting from the fundamental point of view, because one expects that the magnetic behaviour of these dots is different from that of bulk materials, continuous films and even ellipsoidal particles, due to the inhomogeneous internal magnetic field. In addition any realistic estimate of static and dynamical magnetic properties must take both dipolar and exchange interactions into account. From the experimental point of view, a large amount of data has been made available thanks to the improvements in the techniques for sample fabrication (lithography, focused ion beam, nanoimprinting) that have made it possible to produce these small structures with precision and reproducibility [2–6], and to the advances in instrumentation for the observation of magnetic domains [7], and for spin modes measurements [8–13]. Last but not least, the potential technological importance of these systems as storage media and in spin transfer devices has resulted in a continuous effort to decrease their size down to a few hundreds (even tens) of nanometres, in order to increase the density of the dots arrays.

The state of the art of the magnetic normal mode calculations presents a broad scenario. One can distinguish between analytical and numerical methods. The former ones have achieved some success, but in general require certain assumptions regarding the interactions to be taken into account, the boundary conditions and the form of the eigenvectors [14–18]. Actually the pioneering work in this field dates back to the 1950s [19]; we consider here the recent literature only. The numerical methods rely on application of micromagnetics [20]. Most simulations are performed in the time domain, by integrating the Landau–Lifshitz–Gilbert equation with negligible damping and then performing the Fourier transform of selected components of the magnetization. In this way one obtains the spectrum of certain spin excitations and also the mode profiles. These methods are particularly useful to compare with the experimental results obtained in ferromagnetic resonance techniques [10, 11] and in time-resolved Kerr microscopy [8, 9]. Usually such simulations are performed by exploiting the available codes originally designed for the calculation of the ground state of a magnetic particle [21, 22], or derived from them. Other methods have been devised to directly calculate the frequency of the spin excitations, by solving the linearized Landau–Lifshitz equation in the framework of micromagnetism. Such an approach has been used by Boust and Vukadinovich [23] to study the response of a magnetic disc to an external rf field, and by Roussigné *et al* [24] to compute various magnetic modes oscillating across a stripe, modelled as a two-dimensional mesh of triangular elements. The authors of the present paper, and co-workers, have developed a method, called the dynamical matrix method [25], which allows us to derive the frequencies and profiles of the spin normal modes from the subdivision of the particle in cells and the solution of an eigenvalue problem. The elements of the matrix to be diagonalized can be written analytically taking all the interactions (Zeeman, dipolar, exchange) into account and evaluated for any given equilibrium state. Afterwards, standard numerical techniques can be used to find eigenvalues and eigenvectors of the dynamical matrix.

In this paper we present the results obtained by the theoretical group of the University of Ferrara and co-workers, concerning the calculation of the spin normal modes in planar ferromagnetic nanoparticles of various shapes, within both numerical and analytical approaches. The calculated frequencies of the normal modes are compared with the available experimental results for spin excitations in thermal equilibrium, measured at the GHOST Laboratory of the University of Perugia [26] by means of Brillouin light scattering (BLS).

The paper is organized as follows. In section 2 we outline the theoretical approaches and introduce the mode symmetry and nomenclature. In sections 3 and 4 we present the calculated results and compare them to the experimental data for circular and elliptical planar dots, respectively. Conclusions are drawn in section 5.

2. Theory of spin modes

There are different methods to calculate the spin modes in micrometric or nanometric ferromagnetic particles. Essentially they can be grouped in two families: those in the time domain, based of the integration of the Landau–Lifshitz equation for the magnetization and subsequent Fourier transform of certain magnetization components into the frequency domain (giving the excitation spectrum), and those based on the direct evaluation of frequencies and profiles of the spin modes. In this section we introduce methods developed by the authors, belonging to the latter family.

2.1. Micromagnetic modelling: the dynamical matrix method

The spin normal modes of a magnetic nanoparticle can be calculated by using the dynamical matrix method [25, 27, 28]. Within this approach, the particle is divided into N cells within

which the magnetization is assumed constant; therefore, the $2N$ variables of the problem are the two polar angles ϕ_k and θ_k of the magnetization in each cell k. The Zeeman, exchange, and dipolar interactions within the particle are taken into account, and a linearized dynamical matrix, whose eigenvalues correspond to the spin mode frequencies, can be set up. The mode profiles (Cartesian or polar components of the dynamical magnetization) can be derived from the eigenvectors.

Assuming a reference frame with the z-axis along the normal to the surface of the particle, the (unitary) vector specifying the magnetization direction in the cell k is given, in Cartesian coordinates, by

$$\boldsymbol{m}_k = (\sin\theta_k \cos\phi_k, \sin\theta_k \sin\phi_k, \cos\theta_k). \tag{1}$$

It can be shown [25] that the time evolution of the magnetization in each cell, described by the fluctuations from equilibrium of the polar angles $\delta\phi_k$ and $\delta\theta_k$, is governed by the following system of equations:

$$\begin{aligned} \frac{\partial \delta\phi_k}{\partial t} &= -\frac{\gamma}{M_s \sin\theta_k} \sum_{j=1}^{N} \left(E_{\theta_k\phi_j} \delta\phi_j + E_{\theta_k\theta_j} \delta\theta_j \right) \\ \frac{\partial \delta\theta_k}{\partial t} &= \frac{\gamma}{M_s \sin\theta_k} \sum_{j=1}^{N} \left(E_{\phi_k\phi_j} \delta\phi_j + E_{\phi_k\theta_j} \delta\theta_j \right) \end{aligned} \tag{2}$$

where the quantities $E_{\alpha\beta}$ are the second derivatives, at equilibrium, of the energy density E with respect to the angles α and β, M_s is the saturation magnetization and γ is the gyromagnetic ratio. Consistently, the energy density is given by

$$E = \tfrac{1}{2} \sum_{n=1}^{N} \sum_{j=1}^{N} \left(E_{\phi_n\phi_j} \delta\phi_n \delta\phi_j + 2E_{\phi_n\theta_j} \delta\phi_n \delta\theta_j + E_{\theta_n\theta_j} \delta\theta_n \delta\theta_j \right). \tag{3}$$

By introducing the time dependence of the variables as $e^{-i\Omega t}$ and rearranging some terms, we finally get the linear and homogeneous system:

$$\begin{aligned} &\sum_{j=1}^{N} \left(-\frac{E_{\theta_k\phi_j}}{\sin\theta_k} \right) \delta\phi_j + \sum_{j=1}^{N} \left(-\frac{E_{\theta_k\theta_j}}{\sin\theta_k} \right) \delta\theta_j - \lambda\, \delta\phi_k = 0 \\ &\sum_{j=1}^{N} \frac{E_{\phi_k\phi_j}}{\sin\theta_k} \delta\phi_j + \sum_{j=1}^{N} \frac{E_{\phi_k\theta_j}}{\sin\theta_k} \delta\theta_j - \lambda \delta\theta_k = 0 \end{aligned} \tag{4}$$

where $\lambda = -iM_s\Omega/\gamma$. The $2N \times 2N$ matrix A of the system can be defined as

$$\begin{aligned} A_{2k-1,2j-1} &= \frac{E_{\theta_k\theta_j}}{\sin\theta_k}, & A_{2k-1,2j} &= \frac{E_{\theta_k\phi_j}}{\sin\theta_k} + \lambda\delta_{jk}, \\ A_{2k,2j-1} &= \frac{E_{\phi_k\theta_j}}{\sin\theta_k} - \lambda\delta_{jk}, & A_{2k,2j} &= \frac{E_{\phi_k\phi_j}}{\sin\theta_k}. \end{aligned} \qquad k = 1 \ldots N,\ j = 1 \ldots N.$$

In the physical case of real Ω, the matrix is complex; although the Schwarz theorem applies to the energy derivatives, which therefore form a symmetric matrix, the above definition clearly shows that the matrix A is not Hermitian, due to the $\sin\theta_k$ terms. Only if all the θ_k are equal, which occurs for example when the static magnetization lies in-plane in every cell, does the matrix become Hermitian. The system (4) admits non-trivial solutions when $\det A(\lambda) = 0$. This condition is usefully expressed in terms of a new matrix B, defined as

$$\begin{aligned} B_{2k-1,2j-1} &= -A_{2k-1,2j} + \lambda\delta_{jk}, & B_{2k-1,2j} &= -A_{2k-1,2j-1}, \\ B_{2k,2j-1} &= A_{2k,2j}, & B_{2k,2j} &= A_{2k,2j-1} + \lambda\delta_{jk}, \\ & k = 1 \ldots N,\ j = 1 \ldots N, \end{aligned}$$

because in this case it results in an eigenvalue problem for the matrix B:

$$\det(B - \lambda I) = 0$$

and, from the point of view of numerical calculation, an eigenvalue/eigenvector problem is much more easily solved than a root-finding problem. Due to the rearrangement of columns, the real matrix B has no special symmetry. Apart from a multiplicative constant, the eigenvectors $\boldsymbol{v}$ of the problem yield the actual fluctuations of the variables: $\boldsymbol{v} = (\delta\phi_1, \delta\theta_1, \delta\phi_2, \delta\theta_2, \ldots)$.

Once the eigenvectors are calculated, it is possible to obtain the dynamical magnetization $\delta\boldsymbol{m}$ in Cartesian coordinates according to the expression

$$\delta\boldsymbol{m}_k = (-\sin\theta_k \sin\phi_k \delta\phi_k + \cos\theta_k \cos\phi_k \delta\theta_k, \sin\theta_k \cos\phi_k \delta\phi_k + \cos\theta_k \sin\phi_k \delta\theta_k, \\ -\sin\theta_k \delta\theta_k).$$

It must be remarked that $\delta\boldsymbol{m}_k$ is a complex vector, because $\delta\phi_k$ and $\delta\theta_k$ are, in general, complex. A particularly interesting common case corresponds to an in-plane magnetized particle, where $\cos\theta_k = 0$ and $\sin\theta_k = 1$; in this case, after some algebra, it can be shown that the solution has the form $\boldsymbol{v} = (\mathrm{i}\widehat{\delta\phi}_1, \delta\theta_1, \mathrm{i}\widehat{\delta\phi}_2, \delta\theta_2, \ldots)$, where the amplitudes $\widehat{\delta\phi}_k$ and $\delta\theta_k$ can be taken as purely real. In other words the z-components of $\delta\boldsymbol{m}_k$ are in antiphase with the in-plane (x and y) components.

The energy derivatives contain a sum of Zeeman E_z, exchange E_{exc}, and dipolar E_{dip} energies. The Zeeman contribution is

$$E_z = -M_s \boldsymbol{H} \cdot \sum_{j=1}^{N} \boldsymbol{m}_j, \tag{5}$$

where $\boldsymbol{H}$ is the external field. The second derivatives are

$$E_{z\alpha_k\beta_j} = \begin{cases} -M_s \boldsymbol{H} \cdot \dfrac{\partial^2 \boldsymbol{m}_k}{\partial\alpha_k \partial\beta_k} & k = j, \\ 0 & k \neq j. \end{cases}$$

For the exchange,

$$E_{exc} = \frac{A}{d^2} \sum_{j=1}^{N} \sum_{n} (1 - \boldsymbol{m}_j \cdot \boldsymbol{m}_n), \tag{6}$$

where the second sum is carried out over the nearest neighbours of cell j, A is the exchange coupling constant, and the effective exchange strength scales as d^{-2}. The second derivatives are

$$E_{exc\alpha_k\beta_j} = \begin{cases} -\dfrac{2A}{d^2} \displaystyle\sum_{n=1}^{4} \frac{\partial^2 \boldsymbol{m}_k}{\partial\alpha_k \partial\beta_k} \cdot \boldsymbol{m}_n & k = j, \\ -\dfrac{2A}{d^2} \dfrac{\partial \boldsymbol{m}_k}{\partial\alpha_k} \cdot \dfrac{\partial \boldsymbol{m}_j}{\partial\beta_j} & k \text{ and } j \text{ nearest neighbours} \\ 0 & k \text{ and } j \text{ far away.} \end{cases}$$

The dipolar energy can be written through the use of the demagnetizing tensors $\overleftrightarrow{N}(k, j)$, i.e. [29, 30]

$$E_{dip} = \frac{M_s^2}{2} \sum_{k=1}^{N} \sum_{j=1}^{N} \boldsymbol{m}_k \cdot \overleftrightarrow{N}(k, j) \boldsymbol{m}_j. \tag{7}$$

It should be noted that the latter expression is particularly useful within our approach, because the derivative of the energy applies only to the moments $\boldsymbol{m}$, since the demagnetizing

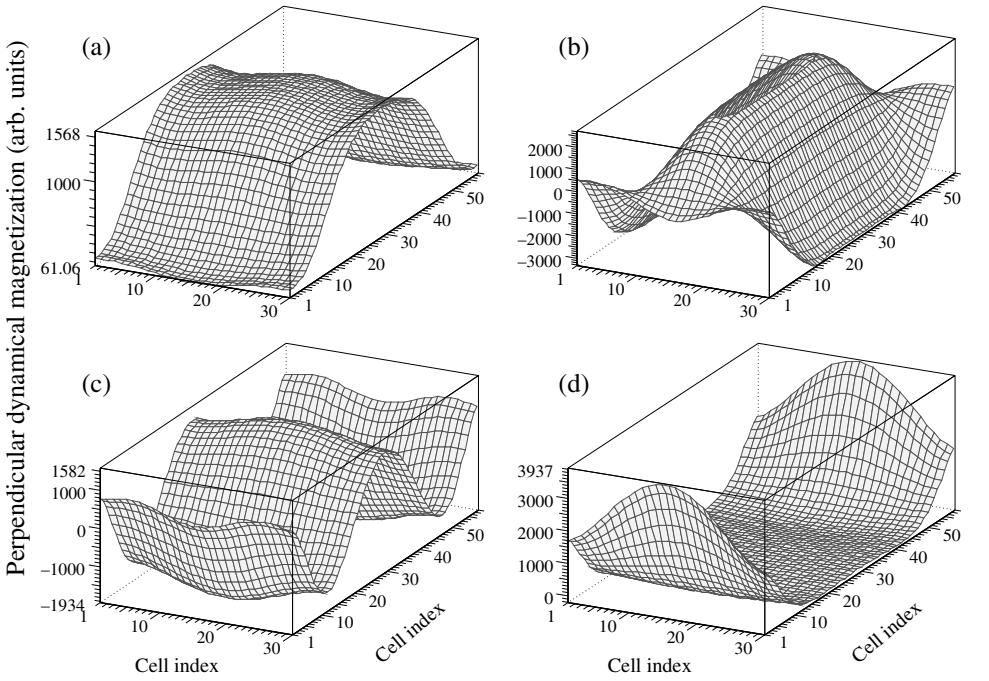

Figure 1. Magnetization profiles (real part of the perpendicular dynamic magnetization) of the F (a), 2-DE (b), 2-BA (c), and 0-EM mode (d) calculated for a rectangular particle.

tensors depend exclusively on the geometry and discretization of the magnetic particle. The demagnetizing tensor is calculated by evaluating the interactions of the magnetic surface charges from every cell (produced by the uniform magnetization inside each cell). Explicit expressions for $\overleftrightarrow{N}$ can be found in [29]; this is also the approach used by default in the OOMMF code [21].

The second derivatives of the dipolar energy are calculated taking into account that the symmetric demagnetizing tensor satisfies $\overleftrightarrow{N}(k,j) = \overleftrightarrow{N}(j,k)$; the result is

$$E_{\mathrm{dip}\alpha_k\beta_j} = \begin{cases} M_\mathrm{s}^2 \left(\displaystyle\sum_{n=1}^{N} \boldsymbol{m}_n \cdot \overleftrightarrow{N}(n,k) \frac{\partial^2 \boldsymbol{m}_k}{\partial\alpha_k \partial\beta_k} + \frac{\partial \boldsymbol{m}_k}{\partial\alpha_k} \cdot \overleftrightarrow{N}(k,k) \frac{\partial \boldsymbol{m}_k}{\partial\beta_k} \right) & k = j \\ M_\mathrm{s}^2 \dfrac{\partial \boldsymbol{m}_k}{\partial\alpha_k} \cdot \overleftrightarrow{N}(k,j) \dfrac{\partial \boldsymbol{m}_j}{\partial\beta_j} & k \neq j. \end{cases}$$

The partial derivatives of the magnetization, which appear in the equations presented in this section, can be easily derived from equation (1) and evaluated at equilibrium.

2.2. Symmetry properties of the normal modes in simple dots

In this subsection we present some typical mode profiles calculated within the dynamical matrix approach, useful for introducing the basic symmetry properties of the modes and the nomenclature used in the paper. The first structure taken into consideration is a rectangular iron element with a quasi-uniform magnetization, obtained by placing the 116 nm × 60 nm × 20 nm particle in an external field of 10 kOe [25]. The profiles of some low-frequency normal modes are shown in figure 1; the field is applied along the long side. Figure 1(a) shows the fundamental

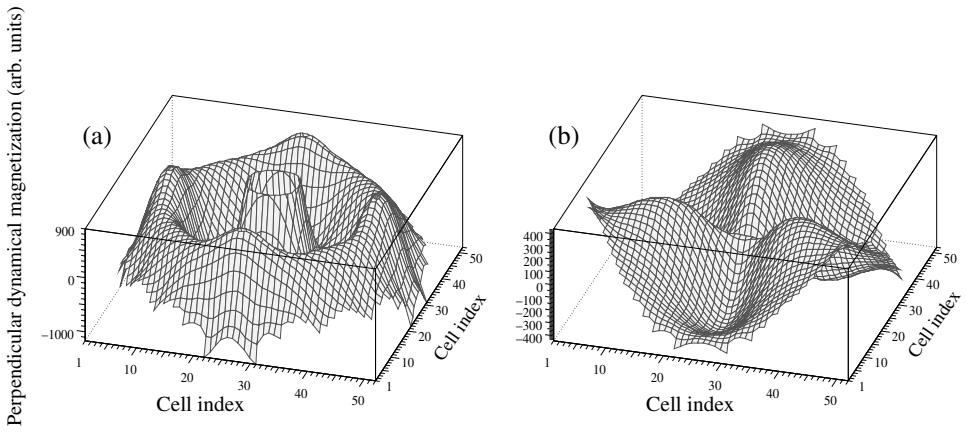

Figure 2. Magnetization profiles (real part of the perpendicular dynamic magnetization) of the (0, 3) (a) and (3, 0) mode (b) calculated for a circular particle in the vortex state.

mode of the system, labelled F; the dynamical magnetization is positive and almost uniform along the direction perpendicular to the field; we note that, moving toward the borders along the direction of the applied field, the amplitude of the mode tends to zero (i.e. the mode is pinned in this direction). A class of modes shows oscillations in the direction perpendicular to the applied field; due to the similarity of these modes with the Damon–Eshbach (DE) mode of continuous films [31], we label them n-DE, where n is the number of nodes; the 2-DE mode is plotted in figure 1(b). Analogously, the modes that oscillate along the direction of the applied field resemble the backward modes of films [31] and are labelled n-BA; the 2-BA mode is plotted in figure 1(c). Finally, figure 1(d) shows the profile of a mode localized at the border of the dot, due to the strong inhomogeneity of the demagnetizing field at the ends of the particle in the direction of the applied field [18]. There is a variety of modes of this kind, called end modes (EMs), which oscillate in the direction perpendicular to the applied field; they are labelled n-EM, where n is the number of nodes. These modes, observed in rectangular elements, can also be found in dots of different shape (e.g. cylindrical dots of circular and elliptical cross section) whenever they are in a saturated quasi-single-domain state. The EMs can be either symmetric or antisymmetric with respect to the plane orthogonal to $\boldsymbol{H}$ and passing through the dot centre.

Dots in the vortex state exhibit different symmetries with respect to saturated ones, so they require an alternate description and different labelling. We consider here the prototype of dots in the vortex state, i.e. circular dots at zero field. In this case the vortex configuration is the equilibrium state of the disc, provided that the aspect ratio lies in a suitable range [32]. In the vortex state the static magnetization forms a curling structure, with a small central core where the magnetization acquires a perpendicular component. Due to the symmetry of the system, the spin excitations exhibit nodal lines that are either parallel (radial modes) or perpendicular (azimuthal modes) to the magnetization; a mode can also show both kinds of nodal line (mixed modes). We use the mode nomenclature (m, n), where m is the node number for azimuthal modes and n the node number for radial modes. For $m = 0$ the profiles have only a radial dependence, while for $n = 0$ the magnetization exhibits both an angular dependence and a radial dependence (without radial nodes); an example of these two cases is shown in figure 2. The calculation refers to a permalloy cylinder with thickness 15 nm and radius 100 nm. The profile of the (0, 3) mode, shown in figure 2(a), crosses the zero-plane along three concentric circles; the plot also evidences a central spike in the vortex core (clipped). Three nodal lines along the dot

diameter, together with three maxima and three minima, characterize the (3, 0) mode, shown in figure 2(b).

The application of an external magnetic field breaks the symmetry of the vortex state. However, we will show in section 3 that the mode labelling, introduced here in the absence of field, can be retained in most cases, following with continuity the deformation of the mode profiles as the field increases. Also the modes of a ring in the vortex state can be classified according to the nomenclature used for a disc. In addition, in a disc, there are modes localized in the region of the vortex core (gyrotropic modes) which represent the motion of the core itself.

2.3. Analytical models for discs

Analytical models developed to study confined magnetic systems can provide important physical insight to better understand the dynamical properties of magnetic dots of different shapes. One of the main problems is to find effective methods for approximating the non-local magnetostatic interactions, in order to provide eigenfrequencies to be compared to inelastic light scattering and ferromagnetic resonance data. Since in general exact analytical solutions of the linearized equation of motion do not exist, a formidable task consists of finding trial eigenfunctions, realistic for the magnetic equilibrium state. Another difficult problem is to find boundary conditions appropriate for a given static equilibrium configuration (vortex or mono-domain) from which it is possible to determine the spin mode wavenumber quantization.

We present here a brief description of the analytical model, formulated for the vortex-state ferromagnetic cylindrical dots in the absence of applied field, that was developed by Zivieri and Nizzoli [16]. The aim of the model is to determine the spin excitation spectrum without limiting assumptions. In fact, the dots studied have a moderate aspect ratio $\beta = L/R < 1$ and dot radius R ranging from the nanometric to the submicrometric scale. L is the dot thickness. Compared to previous recent approaches [15, 33], in this model the following contributions have been considered: (i) the core (C) effective field, (ii) the dynamical exchange field in the whole dot, (iii) both volume and surface charge contributions in the out-of-core (OC) region without any 'ultrathin-dot' approximation, and (iv) the dependence of the dynamical magnetization on the z-coordinate perpendicular to the dot plane. The dynamical dipolar fields have been calculated using the local approximation that may be considered valid for thin dots, but it progressively deteriorates on increasing the dot aspect ratio. The calculated C and OC field contributions are substituted into the linearized equations of motion. It has been proved that the trial eigenfunctions proposed by Ivanov and Zaspel [15] remain valid also in the present model, where dipolar fields are also included and the dots are in the nanometric and submicrometric range. It has been found that the radial part of the eigenvectors of the low frequency (azimuthal) modes are given by Bessel functions of order m equal to or greater than one, while the eigenvectors of the radial modes are given by zero-order Bessel functions. Finally, the model permits us to evaluate the role of the static C exchange field and of the dynamical dipolar C field on the spin dynamics, especially for dots of small radii in the nanometric range. In the next section a quantitative comparison with the dynamical matrix method applied to permalloy cylindrical dots will be presented.

We now present an analytical model formulated for thin cylindrical dots in the saturated state [34]. A group of theoretical studies on the spin dynamics in a uniformly magnetized state has been done on axially magnetized confined systems in the magnetostatic limit [35] and also including exchange interaction [36–38].

Instead, significant difficulties have been encountered for the problem of cylindrical dots in the in-plane saturated configuration. In pioneering works [12, 14] a partial description of the quantized modes of saturated cylindrical dots has been performed using strong approximations

in the demagnetizing field calculation and in the boundary conditions. Even though, recently, the dynamical matrix method [27], discussed in the previous subsections, has been able to shed light on the dynamical magnetic properties in confined systems on nanometric scale, up to now no analytical models have been formulated to describe in a unitary way the normal modes in saturated dots. Hence, the variational method [34] has been proposed to fulfil this need. We present now a brief outline of this theory.

The first step consists of building up the variational functional from the linearized equations of motion and from realistic trial eigenfunctions. Moreover, new boundary conditions obtained for each family of modes must be fulfilled in the presence of dynamical pinning. These boundary conditions, which include both dipolar and exchange terms, remain valid when the internal rotational symmetry is lacking due to in-plane saturation. In particular, the method has been implemented for studying the spin dynamics in tangentially magnetized thin cylindrical dots where both micromagnetic calculations and experimental data were available. In order to construct suitable trial functions for each family of normal modes, it is sufficient to consider a single normal mode in the form of a stationary wave. Since the in-plane magnetization breaks the axial symmetry it is unrealistic to represent the eigenfunctions in terms of single radial Bessel functions times their corresponding angular part as for the vortex state. Therefore, the trial solutions of the equation of motion are written as truncated expansions of cylindrical Bessel functions of increasing order, which represent stationary waves characterized by an in-plane wavenumber with prevalent components along either the x- or the y-axis (k_x or k_y) or both.

The demagnetizing factor, which depends on the in-plane coordinates, is analytically calculated and in general is different for each mode. The mode eigenfrequencies are determined from the solution of the integrals appearing in the variational functional. The quantized wavenumber for the different modes is obtained from the boundary conditions. The variational approach also predicts the existence of end modes observed in thin stripes [17], rectangular [18] and cylindrical dots [12]. The symmetry character and classification of these modes were introduced in the previous subsection. In the analytical model of Jorzick *et al* [18], these modes were derived by assuming a resonance quantization condition of the (real) mode wavenumber in the region where the internal field is highly inhomogeneous. In cylindrical dots, the variational method provides a consistent analytical theory also for these modes, by introducing a complex wavenumber whose imaginary part is proportional to a localization parameter ϵ. The minimization of the variational functional with respect to the variational parameter ϵ gives the value of ϵ which determines the frequency of the end mode.

3. Spin excitations in cylindrical dots

In this section we study spin excitations for cylindrical dots and make a comparison with the BLS experimental results. The sample was grown and patterned at the Institute for Chemical Research of Kyoto University, and consists of a square array of cylindrical dots (ferromagnetic permalloy, $Ni_{81}Fe_{19}$) with nominal thickness $L = 15$ nm, radius $R = 100$ nm and separation $2R$. The array was prepared by means of electron-beam lithography and evaporation in ultrahigh vacuum using an electron-beam gun [12]. The BLS experiments were carried out at the GHOST laboratory [26] (University of Perugia) using a Sandercock $(3 + 3)$-pass tandem Fabry–Perot interferometer. P-polarized light, from a solid state laser operating at $\lambda = 532$ nm, was focused onto the surface of the sample with a power of about 300 mW, with a spot size of about 20 μm. Therefore average properties of a large number of dots are measured in the experiment. A very high signal-to-noise ratio was found in the BLS experiments, with acquisition times about twice those of the continuous film. The external magnetic field, in the

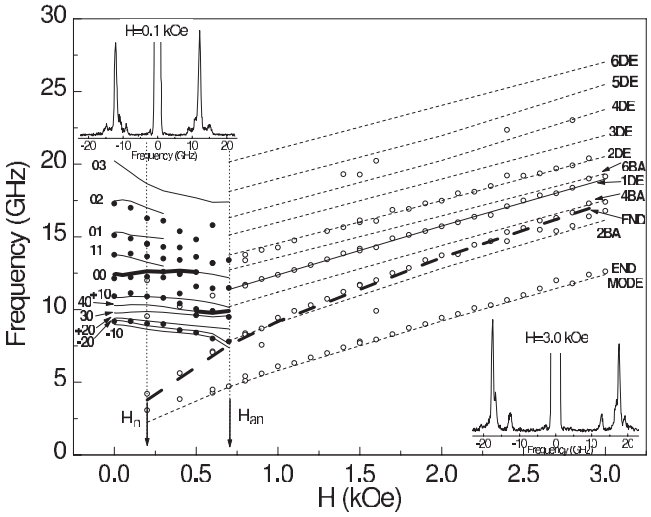

Figure 3. Experimental BLS frequencies: full symbols represent vortex modes, open symbols modes in the saturated state. Calculated frequencies of the modes with the largest BLS cross sections are denoted by the full and dashed lines, in the vortex and saturated states respectively. The bold lines mark the calculated mode associated with the predominant spectral line at any given field (see also insets). Two examples of BLS spectra are shown in the insets. Here FND labels the fundamental mode.

range 0–3.0 kOe, was applied in the plane of the dot array and perpendicular to the scattering plane.

3.1. Results in micromagnetism

The results of the application of the dynamical matrix method to thin cylindrical dots of circular cross section are reported here, together with a detailed comparison with BLS experimental data [27].

In the micromagnetic simulation the magnetic dot is subdivided into a large number $N = 2128$ of cells (parallelepipeds) of square base (side $d = 3.85$ nm) and height L. The interdot dipolar interaction is assumed negligible, so the calculations refer to a single dot. At each applied field, the ground state was calculated by using OOMMF [21]. The material parameters used in the calculation are $M_s = 800$ G for the saturation magnetization and $A = 0.8\ \mu\text{erg cm}^{-1}$ for the exchange stiffness.

In figure 3 we show the experimental results (symbols) and a selected number of calculated low-frequency spin excitations (lines). We discuss the calculated results in three distinct regimes: (a) the vortex state at zero field, with its core at the dot centre [6], (b) the vortex state at finite fields up to the annihilation field $H_{an} = 700$ Oe, and (c) the saturated state. The hysteresis cycle is not fully reversible as measured by the Kerr effect [27]. The saturated dot state persists as a metastable state down to the nucleation field $H_n \approx 200$ Oe. The resolution of the BLS measurements and the small size of these dots allow us to find a larger number of quantized modes with respect to other BLS measurements present in the literature [33, 39].

(a) *Vortex state at zero field.* The symmetry of this state requires that the eigenvectors be of the form [15]

$$\delta\theta_{mn}(\boldsymbol{r}, t) = f_{mn}(r)\mathrm{e}^{\mathrm{i}(m\phi+\omega_{mn}t)} \tag{8a}$$

$$\delta\phi_{mn}(\boldsymbol{r}, t) = \mathrm{i}g_{mn}(r)\mathrm{e}^{\mathrm{i}(m\phi+\omega_{mn}t)} \tag{8b}$$

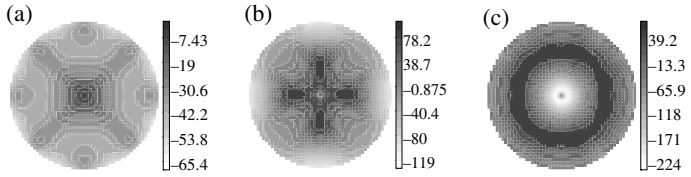

Figure 4. Figures (a)–(c) are the calculated real parts of δm_z for radial modes ($n = 0, 1$ and 2, respectively) in the vortex state at $H = 0$.

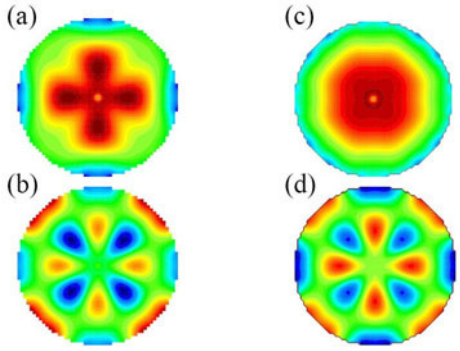

Figure 5. Example of hybridization between vortex modes: the calculated quasi-degenerate modes (a) and (b) are the result of a linear combination of the two ideal stationary-wave-like (0, 1) and (4, 1) modes (c) and (d), respectively.

where f and g are functions of the distance from the centre, m is the azimuthal number, n is the radial number and ω_{mn} is the frequency of a given mode. For $m = 0$ these expressions correspond to mode profiles with only a radial dependence. Our calculations do reproduce a family of modes with these characteristics, whose frequencies increase with increasing number of radial nodes. The functions f_{0n} and g_{0n}, calculated numerically in our scheme, correspond to the results of the analytical model [15, 16] where f and g were taken as combinations of Bessel functions.

In figure 4 we have plotted the amplitude of δm_z, i.e. $-M_s \sin\theta_k \, f_{0n}$, for $n = 0, 1$ and 2. The four-fold symmetry of these modes can be traced to the deviation from cylindrical symmetry caused by creating the disc out of small parallelepipeds. In a few cases, as in figures 4(a), (b), the deviation is enhanced by another very interesting effect, the mode coupling [25]. As an example, the mode profile of figure 4(b) ($n = 1$) results from coupling with the (± 4, 1) modes (see the explanation given in figure 5).

For $m \neq 0$ equations (8) predict a pair of circularly polarized modes for each value of m. In figures 6(a)–(c) we have plotted the profiles of the $(1, 0)$, $(2, 0)$ and $(3, 0)$ modes. Differently from the radial modes ($m = 0$), these modes occur as doublets $\pm m$ and reproduce the expectation of equations (8) yielding two circularly polarized (one clockwise, the other anticlockwise) modes. These modes are non-degenerate in frequency, due to the presence of the out-of-plane component of the vortex core [15], whose direction defines the polarity of the equilibrium state. While the two frequencies of the doublet are independent of the vorticity and polarity of the static magnetization, the sense of polarization of a given mode is determined only by the polarity of the core. Within the $\pm m$ doublet, the mode with highest frequency is clockwise (anticlockwise) polarized for

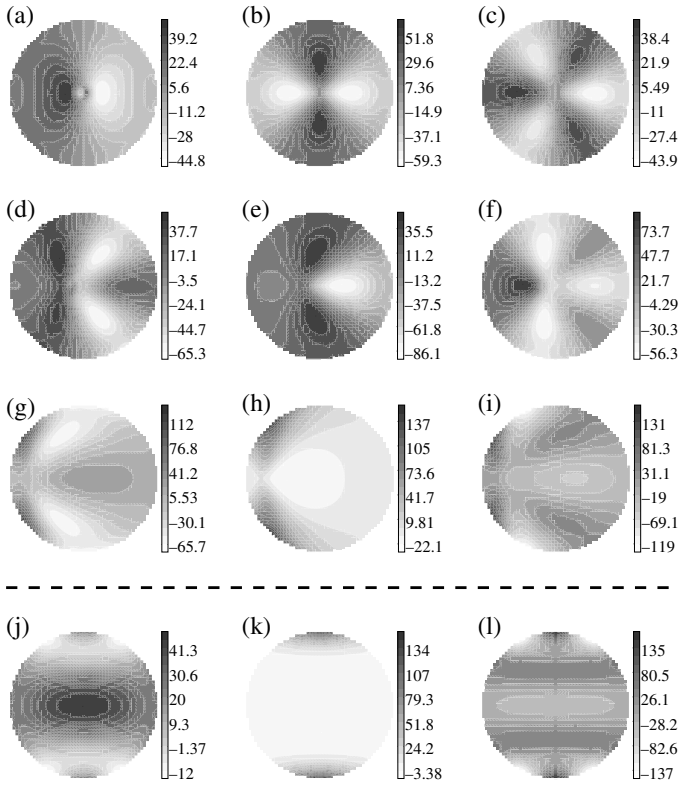

Figure 6. Calculated real part of $\delta m_z(\boldsymbol{r})$ for various modes. Figures (a)–(c) are $m = 1, 2$ and 3 azimuthal modes in a vortex at $H = 0$; their evolution at $H = 0.1$ and 0.7 kOe is shown in (d)–(i). Modes in the saturated state at $H = 0.7$ kOe are shown in (j)–(l), corresponding to the fundamental, symmetric end mode, and 4-BA, respectively. In (d)–(l), the external magnetic field is applied in the plane of the dot array and along the vertical direction of the figure.

positive (negative) vortex polarity. The frequency split of the doublets decreases with increasing m, i.e. the scattering amplitude σ_m of the modes with the vortex core is higher for small m [15]. Finally, looking at the mode profiles, we realize that δm_z can be seen as a combination of Bessel functions of the first (J) and second (Y) type, as predicted in the analytical theory: $J_{m0} \pm \sigma_m Y_{m0}$.

In addition to the kind of spin modes shown in figure 3 and discussed previously, we found another solution at about 0.67 GHz. This low-frequency mode is localized at the dot centre, exhibits an azimuthal nodal line and is circularly polarized. It is referred to as the gyrotropic mode, because it represents the motion of the vortex core as a whole around its equilibrium position, under the action of the gyroforce [40]. This mode is single and its polarization is clockwise (anticlockwise) if the polarity of the ground state is positive (negative). A snapshot of the real part of δm_z is shown in figure 7.

(b) *The vortex state at finite fields.* Although the eigenvectors are no longer given by equations (8), some of the modes can still be labelled by their (m, n) indices at zero field. This can be seen in the mode profiles in figures 6(d)–(f) and (g)–(i), calculated for $H = 0.1$ and 0.7 kOe, respectively. Clearly these modes evolve from those shown in figures 6(a)–(c). The $(0, n)$ radial modes usually undergo hybridization as H varies, so it is not always possible to associate a given mode with a corresponding one at zero field. Finally, the

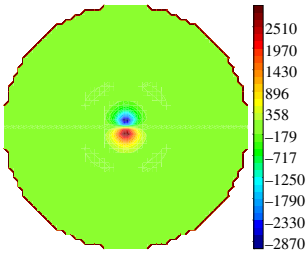

Figure 7. Calculated real part of $\delta m_z(\boldsymbol{r})$ for the gyrotropic mode.

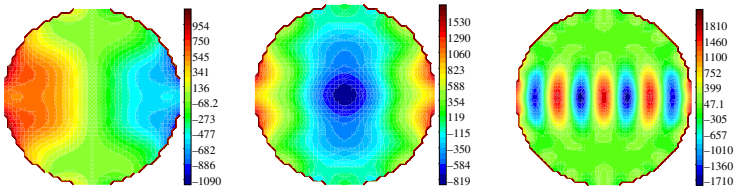

Figure 8. Examples of DE-like modes: from the left, 1-DE, 2-DE, 8-DE.

frequency of the gyrotropic mode is found to vary little with the external field, while its localization shifts from the dot centre.

(c) *Saturated state.* In this case we find modes of the same kind described in section 2.2 for rectangular dots, i.e. Damon–Eshbach-like, backward-like and end modes. In figure 3 we have shown the calculated frequencies of these modes, labelled n-DE or m-BA, where n and m are the number of nodal surfaces. Many modes with nodal lines along both directions are also observed but not shown here. The profile of the fundamental mode of the saturated dot is shown in figure 6(j). An example of a BA-like mode (4-BA) is given in figure 6(l). Examples of DE-like modes are given in figure 8. In addition, we find a pair of low frequency excitations, i.e. end modes (0-EMs), localized at the dot edges in the direction of H. One of these two almost degenerate end modes is symmetric, the other antisymmetric. The profile of the symmetric end mode is shown in figure 6(k).

When the dot is no longer thin, the magnetization may actually vary along the z-axis. In order to allow magnetization oscillations along the z-direction, we divided the dot into five layers parallel to the dot plane, and solved the eigenproblem for dots of different thickness, in the state of vortex magnetization. In figure 9 we plot the frequencies of a few modes in the vortex state as a function of the dot thickness.

In figure 3 we have also presented some information about the BLS cross section. In particular the highest peaks in the calculated spectra are marked by bold lines in the plot of the frequency versus the applied field. The dominant peak in the spectra is, usually, due to the fundamental modes, i.e. the (0, 0) mode in the vortex state and the 0-BA mode in the saturated state.

In order to explain the intensity of the spectral lines, we recall the expression for the backscattering cross section σ, given by

$$\sigma \propto \left| \int\int \left\{ \frac{\sin\theta_i}{\left[\varepsilon_0 - \sin^2(\theta_i)\right]^{1/2}} \delta m_x - \delta m_z \right\} e^{iqx}\, dx\, dy \right|^2, \tag{9}$$

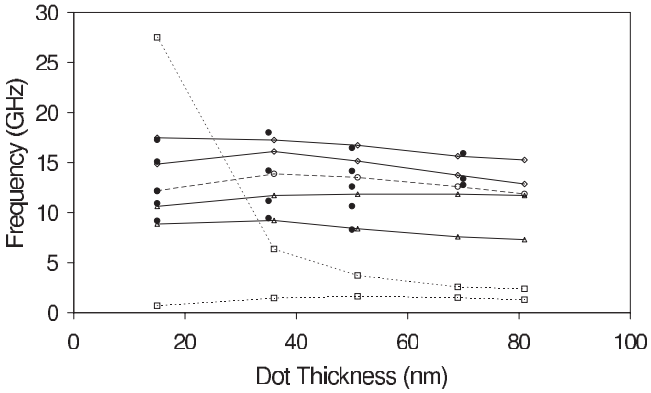

Figure 9. The frequency of a few modes in the vortex state as a function of the dot thickness (radius $R = 100$ nm). Dotted lines with squares refer to the gyrotropic modes (the highest has one nodal surface parallel to the dot plane). From the bottom: lines with triangles are the $(-1, 0)$ and $(+1, 0)$ modes; the dashed line with open circles is the fundamental mode; lines with diamonds are the $(0, 1)$ and $(0, 2)$ modes; full circles are a few experimental BLS data (the BLS data are courtesy of G Gubbiotti and G Carlotti, Perugia).

where ε_0 is the dielectric function of the medium, θ_i is the incident angle of the light and the 2D integral extends over the dot surface [28].

In the present case, the prefactor of δm_x is small, so the leading term in the scattering amplitude is proportional to the Fourier transform of δm_z. In the limit $q \ll L^{-1}$, where L is the length of the dot along the direction of the surface wavevector q, the selection rules for BLS scattering depend upon the symmetry properties of the relevant component δm_z of the dynamic magnetization, because the scattering amplitude is simply given by the average of the δm_z. In the vortex state at zero field, all modes with $m \neq 0$ would not couple; in the saturated state all modes with odd n or m would also have zero coupling.

However, when $qL \approx 1$, the BLS cross section can be appreciable (and in some cases very high) even for odd n-DE-like modes in the saturated state, and for $m \neq 0$ in the vortex state. The agreement between theory and experiment in figure 3 is excellent, not only with regard to the frequency of the modes, but also because the strongest peak in the BLS experiments coincides with the calculated mode with the largest cross section.

In figure 10 we show the calculated frequencies in the vortex state at zero field (full symbols) and the DE-like and BA-like modes in the saturated state for $H = 1$ kOe (open symbols). The similarity between the azimuthal modes in the vortex state and the BA-like modes in the saturated state, and of the radial modes in the vortex with the DE-like modes in saturation, is due to the corresponding orientation of the nodal surfaces relative to the direction of the magnetization. The initial frequency drop in the BA-like and azimuthal modes can be traced to dipolar effects; the subsequent increase is due to exchange.

In order to investigate the effects of the out-of-plane core in the vortex-magnetized discs, we solved the eigenproblem for a disc identical to the previously discussed one, in which however a hole of radius $R_i = 10$ nm was made. As expected, the gyrotropic mode is absent in the calculations, and the $\pm m$ modes are degenerate in frequency and are not circularly polarized. In particular, the degenerate doublet with $m = \pm 1$ is found at about 9 GHz, which corresponds to the frequency of the lowest $(-1, 0)$ mode in the disc. Hence, it can be argued that, in the disc, the mode which is more scattered by the vortex core is the left-handed one.

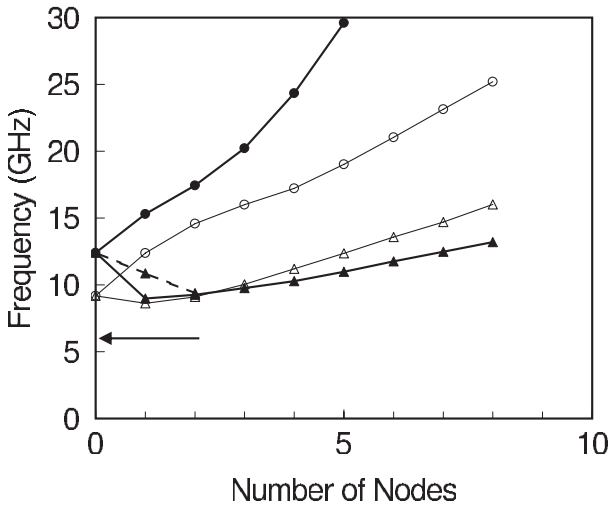

Figure 10. Calculated mode frequencies versus the number of nodes of the real part of δm_z. Full symbols are vortex modes. Circles: $(0, n)$ modes; triangles: $(m, 0)$ modes. The dashed line indicates the splitting of the azimuthal $(\pm m, 0)$ modes. Open symbols are saturated dot modes. Circles: DE-like modes; triangles: BA-like modes. The lines connecting the points are guides to the eye. The horizontal arrow marks the frequency of the end modes of the saturated state.

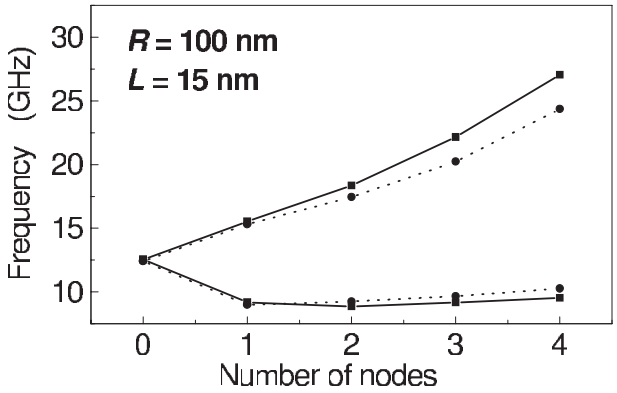

Figure 11. Frequency of the most representative vortex-state modes versus the number of nodes. Continuous line with full squares: dispersion calculated with the analytical model. Dashed line with circles: dispersion calculated with the micromagnetic model. The lines are guides to the eyes.

3.2. Results in the analytical model

In this subsection we present the results obtained within the analytical approach for discs in the vortex state, outlined in section 2.3. The method has been applied to a permalloy dot with $R = 100$ and $L = 15$ nm in order to compare with the numerical results obtained within the dynamical matrix method.

The results of the calculations for the most representative modes are summarized in figure 11. One notes that with both approaches the $m = 0$ radial modes present a frequency dispersion which increases on increasing the number n of the radial nodes, while the dispersion of the $m \neq 0$ azimuthal modes is negative for low m and then, because of the exchange

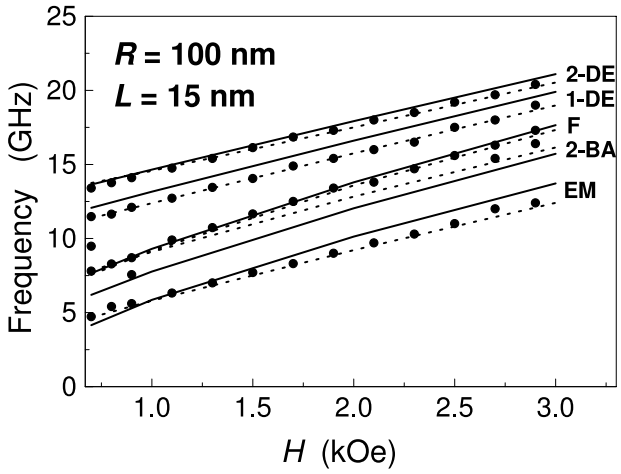

Figure 12. Frequency versus H for a dot with $R = 100$ nm and $L = 15$ nm. Dashed line: micromagnetic calculation. Continuous line: analytical calculation. Circles: BLS data (from Giovannini *et al* [27]).

energy, becomes positive with increasing m. In particular, the calculated mode dispersion with the lowest frequency of the doublet $\pm m$ is depicted. The agreement turns out to be excellent for the azimuthal modes, while for the radial modes there is a difference which is an increasing function of m. In particular, the results of the analytical model are closer to the square power behaviour typical of the non-uniform exchange term. We want now to make a comparison of these results with those obtained in other papers in the literature. In particular, the behaviour of figure 11 is qualitatively and quantitatively different from that obtained by Ivanov and Zaspel [15], where only the exchange field in the long-wavelength limit was taken into account. Another simple model recently developed in micrometric dots including only the dipolar contributions [9] confirms these results, even though these authors assume a different choice of radial eigenfunctions that may be considered plausible for dots in the micrometric range. Furthermore, it is worth noting that in a more recent paper [44] the eigenfrequencies of the doublet ($m = \pm 1$), calculated with the inclusion of the effect of the volume dipolar charges and with non-uniform exchange, are closer to the ones obtained by Zivieri and Nizzoli [16]. Another important result found with the analytical model is the Damon–Eshbach-like positive dispersion of the radial modes and the backward-like negative dispersion of azimuthal modes. This finding is very similar to the one obtained with the micromagnetic approach [27].

We now present a comparison of the results obtained with the variational method [34] with those derived by means of the micromagnetic approach for saturated dots [27]. The dot size and parameters are the same as those considered in the previous subsection. In figure 12 the frequency is shown as a function of the applied field H for the spin modes active in the Brillouin cross section. The overall agreement between the frequencies calculated with the analytical model and those calculated with the dynamical matrix approach is good. Moreover, both methods compare well with the experimental BLS data. Note that the results presented here, obtained with the analytical model, differ only slightly from those presented by Zivieri and Stamps [34] and obtained with parameters fitted to the film data. The agreement with the measured data for the symmetric (2-DE) mode and for the fundamental mode (F) is excellent. As far as the fundamental mode is concerned, i.e. the equivalent of the Kittel uniform mode in ellipsoids [45], in non-ellipsoidal samples this mode dynamical magnetization is large in the

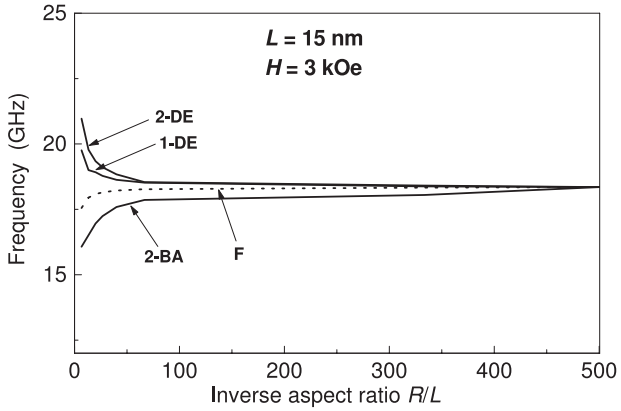

Figure 13. Analytical frequency dispersions of the most representative modes of the spectrum as a function of R/L for a thickness $L = 15$ nm and an applied field $H = 3$ kOe.

centre of the dot and decreases towards the dot edges especially along the direction of the static magnetization **M**, because of the surface pinning (see also figure 1). The energy of this mode is mainly of dipolar nature and its frequency may be found from the approximated formula [34] $(\omega/\gamma)^2 = [H \times [H + 4\pi M_s(1 - 3N_{yy}(\rho = 0))]]$, where H is the external magnetic field and N_{yy} is the demagnetizing tensor components along the static magnetization direction, i.e. y-direction. One notes that the analytically calculated frequency agrees very well also with the micromagnetic one for all the values of H; furthermore, the F mode frequency increases versus H with a different slope with respect to the other modes of the spectrum, because of its almost purely magnetostatic nature.

The analytical model seems to overestimate slightly the experimental frequency of the 1-DE mode and the corresponding micromagnetic calculated frequency. Very likely, this disagreement is due to the effective wavenumber of the stationary wave used in the analytical calculation, which gives a pinned mode, while in micromagnetics it turns out that this mode is unpinned (see figure 8). Since pinning implies a larger effective wavenumber than unpinning, the analytical frequency is higher than the micromagnetic one, due to the exchange interaction.

The symmetric end mode deserves special remarks. The agreement of the micromagnetic calculations with the BLS data in the present case is very good. However, we have found that, in general, the frequency of these modes critically depends on the detailed shape of a dot built up from squared cells. The analytical calculations overestimate the experimental data in the high-field region. A possible source of this discrepancy may be a slight overestimation of the non-uniform exchange field in the variational procedure, because it is evaluated on the dot lateral surface only. Furthermore, in the present model, the variational parameter ϵ is determined at $H = 3$ kOe and the obtained value $\epsilon = 0.8$ is also assumed to be the same in the low-field region. It is important to note that the larger ϵ is, the more the mode is localized.

Finally, in order to show the behaviour of the spin mode dynamics with increasing dot radius, in figure 13 the dependence of the spin wave frequencies of some of the most representative modes on the inverse aspect ratio R/L is depicted for $H = 3$ kOe and for $L = 15$ nm thick dots. Even though there are neither experimental BLS data nor micromagnetic results available for large radii, we believe that it is instructive to study how the spin mode dispersions of confined systems like dots tend towards that of a continuous film [34]. Mode frequencies for small R/L merge asymptotically as the inverse aspect ratio tends to infinity. For $R/L > 400$ they approach the frequency resonance limit of the corresponding continuous film

$\omega = \gamma[H(H + 4\pi M_s)]^{\frac{1}{2}}$. The dispersions of the F and 2-BA modes increase monotonically with increasing R/L, while the dispersions of the 1-DE and 2-DE modes decrease.

4. Spin excitations in elliptical dots

We present here the results of the dynamical calculation on permalloy nanometric elliptical dots. We have chosen to study the effects on the normal modes of dot eccentricity and in-plane direction of the applied field. The results are compared with the experimental BLS data [28].

Details of the preparation were given in section 3. The variation of the dot eccentricity ε was obtained by changing the major axis of the ellipse (a), which assumes the values 200, 300, 400, 500, and 600 nm, and leaving the minor axis (b) fixed to 200 nm, so that the dot eccentricity ($\varepsilon = a/b$) was $\varepsilon = 1.0$, 1.5, 2.0, 2.5, and 3.0. In all the samples the interdot separation is 200 nm in both in-plane directions.

BLS measurements (see section 3) were performed at 1.5 kOe (in order to ensure magnetic saturation of the dots [41]) as a function of ϕ, the angle which measures the direction of the external dc magnetic field with respect to the major axis of the ellipses: $\phi = 0°$ means that $\boldsymbol{H}$ is parallel to the magnetization easy axis of the dots and $\phi = 90°$ means that $\boldsymbol{H}$ is oriented along the short axis of the ellipses. The incidence angle of light θ_i was fixed at 10°, which gives rise to a wavevector parallel to the sample surface $q = 0.41 \times 10^5$ cm^{-1}. Note that this corresponds to a wavelength $\lambda = 2\pi/q$ of 1530 nm, larger than the size of our dots. However, according to the arguments presented in subsection 3.1 λ is not large enough to enforce simple BLS selection rules based on the symmetry/antisymmetry of the eigenvectors.

We first present details on the case of eccentricity $\varepsilon = 2.5$. In our single-dot calculations we neglect the dependence of the magnetization on the dot thickness, which is rather small (15 nm). We use a cell size of $5 \times 5 \times 15$ nm^3, so the elliptical dot with $\varepsilon = 2.5$ is represented by a mesh of 3144 cells. The material parameters used in the calculations are: saturation magnetization $M_s = 800$ G, exchange stiffness constant $A = 1.3$ μerg cm^{-1} and $\gamma/2\pi = 2.95$ GHz kOe^{-1}, where γ is the gyromagnetic ratio. The equilibrium state for the magnetization has been found using OOMMF [21].

Let us consider the simplest cases with highest symmetry when the field $\boldsymbol{H}$ is applied along one of the two axes of the ellipse. The spin modes can be classified with the same nomenclature already introduced in section 2.2. We have therefore end modes (n-EM), where all the amplitude of the modes is localized close to the ellipse edge, backward-like (m-BA) modes, Damon–Eshbach-like (n-DE) modes, and modes with mixed character. The mode with no nodal lines is labelled as the fundamental (F), and it is likely to be the Kittel uniform mode detected in a ferromagnetic resonance experiment (FMR) [45]. It can be seen in figure 14 ($\phi = 0$) that the modes are often hybrids of the 'pure' modes defined above. Similar results were obtained by McMichael and Stiles [42].

Evolution of the mode profiles as the field is applied away from the principal axes is shown in figure 14. In this case, the modes are much less symmetric and hence less easy to group unambiguously into definite categories. Due to the occurrence of hybridization, only a few modes keep their general character at any ϕ. One of these is the EM mode, easy to identify and to follow versus the angle (figure 14). In this case, no other modes of comparable frequency are available for hybridization. Actually, this never happens for the other four modes studied in figure 14. The F mode maintains its character until about $\phi = 50°$, then it strongly hybridizes with a symmetric 0-EM; a similar situation occurs with the 1-DE mode. The 2-BA and 4-BA modes (at $\phi = 0°$) undergo an even stronger modification as the angle changes. 2-BA appears to evolve into a totally antisymmetric end mode (AS 1-EM) when ϕ reaches 90°, and 4-BA gradually becomes a 2-BA mode, with a strong hybridization with a symmetric 4-EM. The

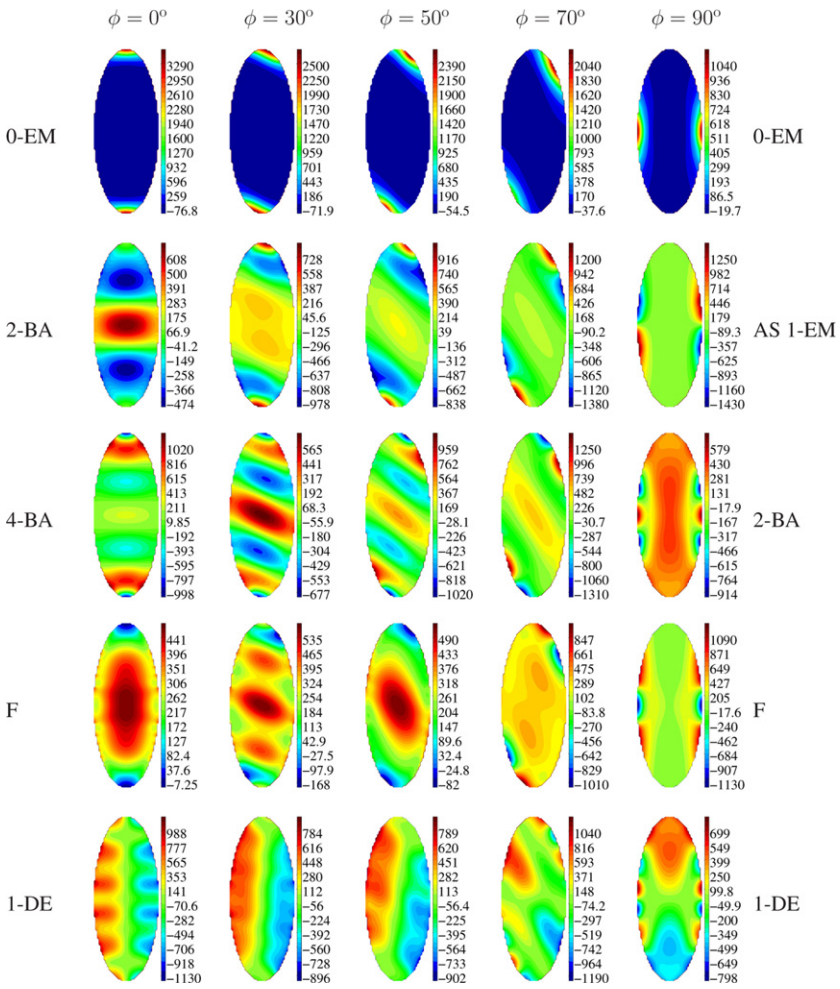

Figure 14. Calculated normal component of the dynamic magnetization Re($\{m_z\}$) of various spin modes plotted versus the angle ϕ between the applied field and the major axis of the ellipses (eccentricity $\varepsilon = 2.5$). The evolution of the modes is tracked according to the continuity of the frequency. The symmetry character of the modes may change close to $\phi = 90°$ (second and third rows); hybridization with end modes may occur (fourth and fifth rows). Figure reprinted with permission from Gubbiotti *et al* [28]. Copyright (2005) by the American Physical Society.

modes, whose real m_z profiles are given in figure 14, are among those responsible for the main peaks in the experimental BLS spectra. As already remarked, the identification of the modes in the spectra requires the knowledge of the BLS selection rules and the evaluation of the cross section.

In figure 15 we plot the measured frequencies of the BLS peaks (symbols) versus the in-plane angle ϕ. Also plotted as lines are the frequencies of the seven modes with appreciable values of the cross section σ, defined by equation (9), which in turn mainly depends on the Fourier transform of m_z for each mode [28]. The evolution of the modes versus ϕ proposed in figure 15 has been based on the angular dependence of the mode profiles shown in figure 14. The dashed lines indicate change of character of a mode and at the same time a vanishing σ. Heavy solid lines refer to values of σ giving rise to the largest peaks in the calculated

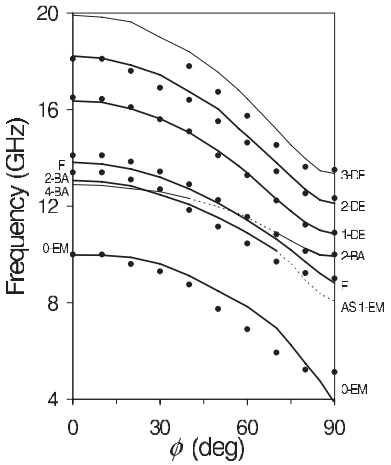

Figure 15. Experimental BLS frequencies (full symbols) for ellipses of eccentricity $\varepsilon = 2.5$, measured versus the angle ϕ between the applied field and the major axis of the ellipses. Full lines specify the calculated frequencies of the modes with appreciable cross section (the heavy lines refer to large cross section). Dashed lines: modes undergoing change of character and exhibiting vanishing cross sections. Figure reprinted with permission from Gubbiotti *et al* [28]. Copyright (2005) by the American Physical Society.

spectra. This representation is only qualitative. Details of the agreement between calculated and measured intensity can be found in Gubbiotti *et al* [28]. To be more precise, for $\phi = 0°$ the cross section due to the F mode is one order of magnitude larger than for the 1-DE, 2-BA, EM modes; for $\phi = 90°$ the calculated σ is large for the 1-DE, 2-BA and F modes (with comparable values), smaller for the EM, very small for the other DE modes, and vanishing for the totally AS 1-EM due to the selection rules.

We stress here that, as explained in section 3, odd modes, such as 1-DE and 3-DE, exhibit an appreciable and detectable cross section, especially when the wavevector $\boldsymbol{q}$ is along the major axis of the ellipse. The good agreement between the simulations and the BLS results allows us to identify with confidence the nature of the modes that are measured.

In figure 15, the frequencies are plotted as a function of the in-plane angle ϕ, and, in general, they all show a monotonic decreasing behaviour. This is because the demagnetizing field increases with ϕ, producing a decrease in the effective magnetic field and a consequent reduction of the mode frequencies. The same happens when considering ellipses of smaller eccentricity (figure 16). The comparison with the calculated curves allows us to distinguish three main groups of spin modes ((a), (b), (c) in the following discussion).

(a) The lowest-frequency mode is assigned as a pure 0-EM. This mode is strongly localized in the direction of the applied field for $\phi = 0°$, $90°$ and at an angle less than ϕ for intermediate angles of the applied field. Indeed, the particle shape anisotropy forces the average particle magnetization to make an angle with the easy axis smaller than ϕ. The agreement between theory and experiment is good only close to the easy axis. We have found that the calculated frequency of the 0-EM mode is strictly related to the curvature of the ellipse edges where the mode is localized. Due to the actual experimental spread of the shape of each dot in the array and the strong dependence of the 0-EM frequency on the dot local curvature, we also expect the BLS experimental peaks of these modes to be rather broad. In addition, in our simulated ellipse, the discretized edge around the hard axis (flat over some distance) is a worse approximation of the actual rounded elliptical profile than

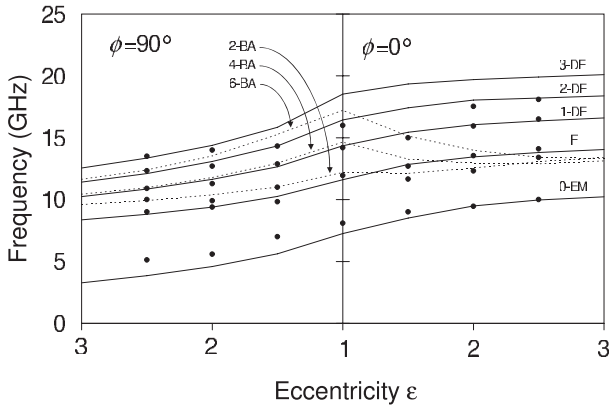

Figure 16. Experimental Brillouin frequencies (full symbols) of various modes plotted versus the eccentricity ε, compared with the calculated frequencies (lines). The results are shown for the applied field along the easy ($\phi = 0°$) and hard axes ($\phi = 90°$). Modes are labelled according to the nomenclature introduced in the text. Full lines: fundamental (F), Damon–Eshbach-like (n-DE) and end modes (n-EM). Dashed lines: backward-like modes (m-BA). Figure reprinted with permission from Gubbiotti *et al* [28]. Copyright (2005) by the American Physical Society.

the easy axis, and this can result in a discrepancy between the measured and calculated frequencies.

(b) The second group of spin modes in the BLS spectra is a doublet in the frequency range 13–14 GHz for $\phi = 0°$ and 9–10 GHz for $\phi = 90°$. In the angular range $\phi = 0°$–$70°$ the two modes are assigned to the fundamental and the 2-BA mode for the upper and lower frequency, respectively. Close to the hard axis ($\phi = 70°$–$90°$) their frequencies cross. In the range $\phi = 50°$–$90°$ all the BA modes undergo deep modifications, mainly because, when ϕ increases, the room for the mode oscillations decreases drastically from the easy (major) axis to the hard (minor) axis. In addition, the modes cross and hybridize. In particular the 4-BA mode (at $\phi = 0°$), in an effort to adjust its oscillations to the decreasing available space when the applied field approaches the hard axis, even loses nodes and becomes the 2-BA mode: this happens close to $\phi = 58°$, which corresponds to the average particle magnetization halfway between the easy and hard axes.

(c) The modes of the third group are DE-like modes with nodal surfaces parallel to the local magnetization, although the analysis of figure 14 shows, for the 1-DE and 2-DE modes, that the magnetization profile is complex and the curves of equal magnetization are rather wiggly. The 1-DE mode is hybridized with the 5-EM for $\phi = 90°$. The DE modes show a simpler behaviour than the BA modes because they do not intersect when plotted as function of ϕ. This is actually due to the different dependence of the frequency of DE and BA modes versus the node number, as analysed in detail by Gubbiotti *et al* [28].

We now present numerical results for different ellipses, in order to investigate in detail the effect of the eccentricity ε on the different modes, as a function of the direction of the applied magnetic field. In figure 16 we give a synoptic representation of the frequency behaviour of the main spin modes versus eccentricity. Experimental and calculated results are shown for values $\varepsilon = 1.0$, 1.5, 2.0, 2.5, and 3.0. The minor axis of the ellipse is kept constant (200 nm).

The overall agreement between the calculated and measured mode frequencies is very good, and confirms the assignment previously done for $\varepsilon = 2.5$. The behaviour versus the eccentricity can be interpreted on the basis of the frequency dependence upon: (1) the

demagnetizing factor, (2) the confinement length $\Delta\lambda$ appropriate to each family of modes, and (3) the ellipse local curvature for the end modes. $\Delta\lambda$ is defined as the size of the dot in the direction of the oscillation of a particular mode. For $\phi = 90°$ an increase of the eccentricity corresponds to a general decrease of the mode frequencies because the demagnetizing factor along the hard axis increases (therefore the effective field decreases), $\Delta\lambda$ remains constant for the BA and increases for the DE modes, and the curvature of the end of the ellipse increases. All these effects produce a frequency decrease versus ε. The same, but reversed, arguments hold at $\phi = 0°$ for the DE and EM modes, while for the BA modes two effects compete. When the exchange is important (as for small ε or high mode index m) an increase of ε produces an increase of $\Delta\lambda$ along the easy axis and a corresponding decrease of the mode wavenumber. Therefore the frequency drops with ε. This is not true for the 2-BA mode, scarcely affected by exchange. In addition, in the limit of high ε, all the m-BA modes tend to the asymptotic magnetostatic value of the infinite stripe [43].

5. Conclusions

The recent advances in experimental techniques have made possible the collection of a large amount of data concerning the frequencies and the profiles of the spin excitations in magnetic planar nanoparticles of different shape, e.g. dots of squared, rectangular, triangular, circular and elliptical cross section, without and with defects, such as holes. In order to assign these excitations, proper and realistic theoretical schemes are required to handle complicated situations such as those arising, for example, when the spin modes are measured versus an external dc field that varies in magnitude and direction.

We have reviewed our theoretical work in the field of spin mode calculations, within both the dynamical matrix method and analytical approaches, applied to circular and elliptical particles. We have shown that the experimental Brillouin light scattering data taken on samples of this kind can be interpreted with the aid of the calculated normal mode eigenvalues and eigenvectors. In particular it is possible to determine the symmetry of the measured excitations and correlate the mode behaviour to the different equilibrium states induced by the field. Finally, a direct comparison between the BLS spectra and the calculated mode frequencies is made possible by the evaluation of the BLS cross section, which can be derived from the knowledge of the mode eigenvectors.

Acknowledgments

We are indebted to G Carlotti, G Gubbiotti and co-workers for the large amount of experimental work on BLS and to M Grimsditch for collaboration in developing the dynamical matrix method. Financial support by Ministero Università e Ricerca (grant PRIN 2004027288) and Università degli Studi di Ferrara (NANO&NANO project) is acknowledged.

References

[1] Hillebrands B and Thiaville A (ed) 2006 *Spin Dynamics in Confined Magnetic Structures III* (Berlin: Springer)
[2] Adeyeye A O, Bland J A C, Daboo C, Hasko D G and Ahmed H 1997 *J. Appl. Phys.* **82** 469
[3] Rousseaux F, Decanini D, Carcenac F, Cambril E, Ravet M F, Chappert C, Bardou N, Bartenlian B and Veillet P 1995 *J. Vac. Sci. Technol.* B **13** 2787
[4] Shearwood C, Blundell S J, Baird M J, Bland J A C, Gester M, Ahmed H and Hughes H P 1994 *J. Appl. Phys.* **75** 3249
[5] Chou S Y, Kraus P R, Zhang W, Guo L and Zhuang L 1997 *J. Vac. Sci. Technol.* B **15** 2897
[6] Shinjo T, Okuno T, Hassdorf R, Shigeto K and Ono T 2000 *Science* **289** 5481

[7] Hubert A and Schäfer R 1998 *Magnetic Domains* (Berlin: Springer)
[8] Park J P, Eames P, Engebretson D M, Berezovsky J and Crowell P A 2003 *Phys. Rev.* B **67** 020403
[9] Buess M, Knowles T P J, Höllinger R, Haug T, Krey U, Weiss D, Pescia D, Scheinfein M R and Back C H 2005 *Phys. Rev.* B **71** 104415
[10] Giesen F, Podbielski J, Korn T, Steiner M, van Staa A and Grundler D 2005 *Appl. Phys. Lett.* **86** 112510
[11] Neudecker I, Kläui M, Perzlmaier K, Backes D, Heyderman L J, Vaz C A F, Bland J A C, Rüdiger U and Back C H 2006 *Phys. Rev. Lett.* **96** 057207
[12] Gubbiotti G, Carlotti G, Okuno T, Shinjo T, Nizzoli F and Zivieri R 2003 *Phys. Rev.* B **68** 184409
[13] Demidov V E, Demokritov S O, Hillebrands B, Laufenberg M and Freitas P P 2004 *Appl. Phys. Lett.* **85** 2866
[14] Guslienko K Yu and Slavin A N 2000 *J. Appl. Phys.* **87** 6337
[15] Ivanov B A and Zaspel C E 2002 *Appl. Phys. Lett.* **81** 1261
[16] Zivieri R and Nizzoli F 2005 *Phys. Rev.* B **71** 014411
[17] Guslienko K Y, Chantrell R W and Slavin A N 2003 *Phys. Rev.* B **68** 024422
[18] Jorzick J, Demokritov S O, Hillebrands B, Bailleul M, Fermon C, Guslienko K Yu, Slavin A N, Berkov D V and Gorn N L 2002 *Phys. Rev. Lett.* **88** 047204
[19] Walker L R 1957 *Phys. Rev.* **105** 390
[20] Brown W F Jr 1978 *Micromagnetics* (New York: Krieger)
[21] Donahue M and Porter D 2002 *OOMMF User's Guide, Version 1.2 alpha 3* (Gaithersburg, MD: National Institute of Standards and Technology)
[22] LLG Micromagnetics Simulator, llgmicro@mindsping.com
[23] Boust F and Vukadinovic N 2004 *Phys. Rev.* B **70** 172408
[24] Roussigné Y, Chérif S M and Moch P 2003 *J. Magn. Magn. Mater.* **263** 289
[25] Grimsditch M, Giovannini L, Montoncello F, Nizzoli F, Leaf G K and Kaper H G 2004 *Phys. Rev.* B **70** 054409
[26] http://ghost.fisica.unipg.it
[27] Giovannini L, Montoncello F, Nizzoli F, Gubbiotti G, Carlotti G, Okuno T, Shinjo T and Grimsditch M 2004 *Phys. Rev.* B **70** 172404
[28] Gubbiotti G, Carlotti G, Okuno T, Grimsditch M, Giovannini L, Montoncello F and Nizzoli F 2005 *Phys. Rev.* B **72** 184419
[29] Newell A J, Williams W and Dunlop D J 1993 *J. Geophys. Res.* **98** 9551
[30] Schabes M E and Aharoni A 1987 *IEEE Trans. Magn.* **23** 3882
[31] Cottam M G and Slavin A N 1994 *Linear and Nonlinear Spin Waves in Magnetic Films and Superlattices* ed M G Cottam (Singapore: World Scientific) p 1
[32] Cowburn R P, Koltsov D K, Adeyeye A O, Welland M E and Tricker D M 1999 *Phys. Rev. Lett.* **83** 1042
[33] Novosad V, Grimsditch M, Guslienko K Yu, Vavassori P, Otani Y and Bader S D 2002 *Phys. Rev.* B **66** 052407
[34] Zivieri R and Stamps R L 2006 *Phys. Rev.* B **73** 144422
[35] Fletcher P C and Kittel C 1960 *Phys. Rev.* **120** 2004
[36] Arias R and Mills D L 2001 *Phys. Rev.* B **63** 134439
[37] Arias R and Mills D L 2004 *Phys. Rev.* B **70** 094414
[38] Kakazei G N, Wigen P E, Guslienko K Yu, Chantrell R W, Lesnik N A, Metlushko V, Shima H, Fukamichi K, Otani Y and Novosad V 2003 *J. Appl. Phys.* **93** 8418
[39] Jorzick J, Demokritov S O, Hillebrands B, Bartenlian B, Chappert C, Decanini D, Rousseaux F and Cambril E 1999 *Appl. Phys. Lett.* **75** 3859
[40] Usov N A and Kurkina L G 2002 *J. Magn. Magn. Mater.* **242** 1005
[41] Carace F, Vavassori P, Gubbiotti G, Tacchi S, Madami M, Carlotti G and Okuno T 2006 *Thin Solid Films* **515** 727
[42] McMichael R D and Stiles M D 2005 *J. Appl. Phys.* **97** 10J901
[43] Jorzick J, Demokritov S O, Mathieu C, Hillebrands B, Bartenlian B, Chappert C, Rousseaux F and Slavin A N 1999 *Phys. Rev.* B **60** 15194
[44] Zaspel C E, Ivanov B A, Park J P and Crowell P A 2005 *Phys. Rev.* B **72** 024427
[45] Kittel C 1948 *Phys. Rev.* **73** 155